Research Article

Damage Process and Fracture Mechanisms in the Rock Surrounding a Roadway Caused by Blasting-Induced Disturbance under High Stress

Gang Lei,[1] Dawei Wu ⓘ,[2] and Xiaozhang Shi[1]

[1]*Faculty of Quality Management and Inspection, Yibin University, Yibin, Sichuan 644000, China*
[2]*Department of Civil Engineering, Chengdu Technological University, Chengdu, Sichuan 644000, China*

Correspondence should be addressed to Dawei Wu; wdwmine@163.com

The aim of this study is to investigate damage processes and fracture mechanisms in the rock surrounding a roadway under blasting-induced disturbance in a high-stress environment. A disturbance test involving blasting of the rock surrounding a roadway under different lateral pressure coefficients was conducted using high-precision acoustic emission (AE) monitoring. Based thereon, the spatiotemporal evolution and cluster characteristics of microcracks in the surrounding rock of the roadway under dynamic disturbance induced by explosive blasting were obtained, and stress transfer, adjustment, and redistribution in the rock mass were revealed. Moreover, a method for describing the progressive damage to the rock mass was established. The conclusions were as follows: the high-stress environment was conducive to microcrack initiation and propagation in the specimens, and the failure patterns of the surrounding rock of the roadway under different lateral pressure coefficients differed. The direction of crack propagation in the rock surrounding the roadway is opposite to that of the maximum principal stress applied to the rock mass. Blasting-induced disturbance intensifies crack initiation and accelerates damage accumulation and macrofracture formation in the rock mass. The macroscopic failure zone in a model is correlated with the ultimate distribution of apparent stress, and the apparent stress can reflect the adjustment of the stress field therein. The damage variable, characterized by the ratio of the number of AE events, can reveal the evolution of damage in the rock surrounding a roadway.

1. Introduction

Under high stress, the development and utilization of deep mineral resources faces increasingly severe disasters caused by blasting-induced disturbance. When the rock surrounding a deep roadway is subjected to extremely high initial stress, a small external disturbance may lead to failure. Blasting-induced disturbance inevitably causes different degrees of damage to a rock mass, making the roadway prone to large-volume caving and collapse, even inducing sudden, destructive dynamic disasters with neither precursor nor warning thereof. Some studies show that two-thirds of surrounding rock failures around mine roadways occur in the period after production and blasting, and rock failure is related to blasting-induced disturbance [1–3]. For example, time-delayed rockbursts occurred in a deeply buried tunnel at Jinping II hydropower station, Sichuan Province, China, due to blasting excavation-induced disturbance, with the damage ranging from 2 to 4 m in height and 30 m in length, and the maximum pit depth was 0.9 m [4]. Due to blasting-induced disturbance in the adjacent stope, massive ore caving took place in the No. 2 stope in the middle section of 0 m and a roadway across the vein in Ashele copper mine (Xinjiang Uygur Autonomous Region, China), with a caved-in mass of 1×10^4 tons and a caving depth of 10 m [5]. A roadway in Daye Iron Mine collapsed under high-strength, blasting-induced disturbance of the surrounding rock, resulting in an economic loss of several million yuan [6]. In recent years, attention has been paid to research into the failure mechanisms of the rock surrounding deep roadways under blasting-induced disturbance.

When the rock surrounding a roadway is subjected to an external disturbance, such as that induced by blasting, many microcracks are initiated that then propagate and coalesce. In the process of disturbance, these microfractures, with different scales and types, gradually change from having a disorderly distribution to a more ordered state, finally forming macrocracks, which lead to the failure of the rock. In physical experiments simulating rock subjected to impact load, the split Hopkinson pressure bar (SHPB) is commonly used to study the mechanical characteristics of rock under blasting-induced disturbance [7–10]. In 1972, by conducting dynamic tests on rock under different confining pressures with the SHPB, Christenson et al. [11] studied the dynamic characteristics of rock under different initial stresses. Since then, many research teams have conducted triaxial impact tests on rock and concrete materials based on the improved SHPB device, so as to investigate mechanical responses and failure characteristics of a variety of types of rock under combined dynamic and static loading conditions. By performing a dynamic disturbance test on Brazilian disk (BD) rock specimens with the SHPB, Ai et al. [8] studied the dynamic mechanical properties of, and crack propagation in, rock under impact load at a high strain rate. Zhou et al. [12] investigated the evolution of microcracks and failure mechanisms in granite under impact load by using an improved SHPB. Based on the SHPB, Du et al. [13] studied dynamic behaviors of granite specimens under different static stress conditions and analyzed dynamic failure modes of rock under different strain rates. In terms of numerical simulation of failure of a rock mass under blasting-induced disturbance, Duan et al. [14] assessed the stability of the rock surrounding the roadway in Anjialing Coal Mine (Shanxi Province, China) before and after blasting through FLAC^{3D} simulation. Moreover, he evaluated the effects of blasting vibration on the stress field, displacement, and plastic zone in the surrounding rock. By using the finite element software LS-DYNA, Jiang and Zhou [15] investigated the influences of blasting vibration on the stability of the rock surrounding a tunnel and stress distributions thereon, establishing a relationship between stress distribution in the tunnel structure and peak blasting vibration velocity. With the aid of particle flow code (PFC) software, Li et al. [16] simulated the dynamic responses of the surrounding rock of an underground tunnel under blast loading and evaluated the dynamic stress concentration factor (DSCF) in the surrounding rock.

The aforementioned studies of the failure process and mechanical characteristics of rock under dynamic disturbance mainly focus on surface observation, while the damage evolution characteristics and adjustment process of stress fields in rock are rarely examined. Acoustic emission (AE) monitoring technology, as a useful tool to study the failure and fracture process of brittle materials, such as rock, can, without interruption to mining operations, be used to monitor the evolution of microcrack initiation, propagation, and coalescence in rock in real time and locate microfractures in a rock mass. Therefore, it has been widely used in research into the failure and fracture mechanisms of brittle heterogeneous materials, such as rock and concrete [17–21]. A disturbance test involving blasting of the rock surrounding a roadway under different lateral pressure coefficients was conducted using high-precision acoustic emission (AE) monitoring. Based thereon, the spatiotemporal evolution and cluster characteristics of microcracks in the surrounding rock of the roadway under dynamic disturbance induced by explosive blasting were obtained, and stress transfer, adjustment, and redistribution in the rock mass were revealed. Moreover, a method for describing the progressive damage to the rock mass was established.

2. Design of Test Schemes

Cement mortar has good uniformity and isotropy, and its strength can be adjusted according to the capacity of the loading equipment. In this research, cement mortar was used as a model material to replace rock. Based on the loading capacity of a mechanical test system under biaxial loading in the laboratory and the model size requirements, a model measuring 300 mm × 300 mm × 250 mm (length × width × height) was designed with a uniaxial compressive strength of 25 MPa. The model (fabricated in cement mortar) was mixed and cast with cement, quartz sand, and water and cured under standard conditions. The curing time of the cement mortar model was 28 days. Also, specimens with the same mass ratio were used to measure the uniaxial compressive strength (UCS), and the results showed that the UCS of this batch of specimens was approximately 25 MPa. Through the test, the density of the test model is 2.1×10^3 kg/m^3, shear strength is about 1.9 MPa, tensile strength is about 2.8 MPa, frictional angle is 32.5°. It was essential to grind and clean the surface of the cement mortar samples after reaching the designed strength of the samples, to guarantee that the surface roughness of the samples conformed to test requirements. After the model reached the design requirements, it was further worked to form the final model. According to the theory of elasticity, when the radius of the roadway is significantly smaller than the depth at which it is buried, the excavated rock mass can be considered as an infinitely elastic body with circular holes experiencing bidirectional compression. Taking into account the Saint-Venant boundary effect principle and the size of the model, a round roadway was formed in the center of the specimen, with a diameter of 57 mm. The distance between the circular hole and the boundary is set to be greater than 5 times the radius of the circular hole to ensure compliance with the experimental requirements. A blast hole was located between the roadway and side wall of the model, some 60 mm from the bottom of the model, with an outer diameter of 8 mm and a length of 125 mm. To reduce the direct effects of the blasting on the specimen, a steel tube was fixed within the blast hole, and the explosive was placed therein. During the explosion, only vibration energy is released externally. Due to the use of circular roadway, stress waves are uniformly released outward after the explosion of explosives. The distance between the blasting hole and the circular roadway has a significant impact on the AE events generated during roadway damage, while the position relationship between the blasting hole and the roadway has a relatively small impact. The explosive used in the test was hexogen and

potassium picrate mixed in a certain mass ratio, and some 1 g of explosive was used in each blasting operation. After charging, the blast hole was filled with fine sand, and the blasting was electrically initiated.

The AE monitoring system (Physical Acoustic Corporation, USA) was utilized in the test. 17 Nano30 AE sensors specific for cement mortar with response frequencies of between 50 and 400 kHz were adopted. Nine and eight sensors were separately arranged in the front and back of the model, and they could monitor all areas near the roadway structure (Figure 1). To ensure that the sensors were coupled to, and in intimate contact with, the specimen, Vaseline™ was smeared over the contact part, and the sensors were then fixed to the specimen with rubber bands. A self-designed automatic hydraulic biaxial loading system was used to apply stress-controlled loading in the test: this system could be used to control both the transverse and longitudinal stresses (Figure 2). During stress loading, it was necessary to place shock-reducing modules at the point of contact between the press ram and the model to reduce friction at the end of the model during loading.

Four blasting-induced disturbance schemes under different initial stress conditions were used; by setting the transverse stress P1 to 16 MPa and adjusting the longitudinal stress P2, the lateral pressure coefficients were set to 0.8, 1.0, 1.2, and 1.4 (Table 1). During the initial stress loading, P1 and P2 were simultaneously applied at a rate of 3 MPa/min. When the transverse stress P1 reached 16 MPa, the load was held, while the longitudinal stress P2 was further increased to the target value of 20 MPa (16, 13.3, and 11.4 MPa). After SE signals were no longer generated within the specimen, six blasting operations were conducted (successive blasts were detonated after the AE signals from the previous blast had ceased). When the AE signals produced by the final blast had been completely attenuated, the next stress increment was applied. In this case, the transverse stress P1 was kept unchanged, while the longitudinal stress P2 was increased until the specimen became unstable and was damaged.

3. AE Location Methods and Verification of Location Accuracy

An autoregressive model was built based on the Akaike information criterion (AIC) to obtain accurate P-wave arrival times, and AE events were located using the Simplex algorithm. Due to the presence of the prefabricated circular hole, the elastic wave will refract and reflect around the prefabricated circular hole, and the time when the sensor receives the signal will change, which will affect positioning accuracy. Therefore, when performing acoustic emission localization calculation, the signal that arrives later is deleted, and the eight sensors that receive the signal first are used in the calculation.

To verify the location accuracy of the Simplex algorithm, the preset location was determined by way of a nail-dropping test, and an autoregressive model was built based on the Akaike information criterion (AIC) to obtain accurate P-wave arrival times. Moreover, the AE events were located with the Simplex algorithm, and the nail-drop

location was compared with the actual location results. By comparing the positioning result with the preset position, it is found that most of the positioning results appear in the area near the predetermined position. The maximum deviation is 16.6 mm, while the minimum is 2.4 mm. More than 90% of the positioning error is controlled within 10 mm, demonstrating an acceptable coincidence and satisfaction on the monitoring precision. The positioning results are shown in Figure 3.

4. Spatiotemporal Evolution and Cluster Characteristics of AE Events

The stress shock wave generated by the explosion propagates within the sample in the form of elastic waves, triggering vibration signals. These vibration signals are captured by AE sensors and doped in rock fracture signals, which can cause certain interference in the positioning and inversion of microcrack signals. The experiment removed the AE signals generated at the moment of explosion and the vibration signals generated by blasting, leaving only the microfracture signals inside the rock mass. When the elastic stress wave generated by the explosion reaches the boundary of the roadway, a portion of the elastic stress wave will transmit through, while another portion will undergo reflection, resulting in the formation of reflected tensile waves that continue to propagate within the specimen. The elastic stress wave propagating within the specimen gradually attenuates during the propagation process. Frictional interaction occurs as the elastic wave propagates along the particle interfaces, leading to the conversion of mechanical energy into thermal energy. This energy is gradually consumed, causing the amplitude and frequency of the elastic wave to continuously decrease. Eventually, the elastic wave energy is completely dissipated, and the amplitude drops below the threshold value for acoustic emission detection. At this moment, the termination time of the propagation process of the elastic stress wave is considered.

In accordance with the model, the location results of AE events obtained in an initial stress stage, a blasting-induced disturbance stage and a later stage of stress loading in the test were shown. The location results of AE events were analyzed by selecting representative specimens M1-3, M2-3, M3-3, and M4-3 (Figure 4). With increasing the initial stress load, the samples undergo stable crack propagation, and the compacted primary cracks start to extend, accompanied by the initiation of new cracks. As the load increases, the samples enter the unstable crack propagation stage, during which numerous new cracks are generated, these then propagate and coalesce. In this case, the AE activity is further intensified. The stable and unstable crack propagation stages are the main stages of the initiation and propagation of cracks in the samples. After initial stress conditions have just stabilized, the stress field in the samples is constantly adjusted and internal cracks and fractures gradually propagate and coalesce. The regional stress recovers, then stabilises, and the AE activity decreases over time.

For the specimen with $k = 0.8$, AE events are distributed around the round roadway, and a few events with high

(a)   (b)
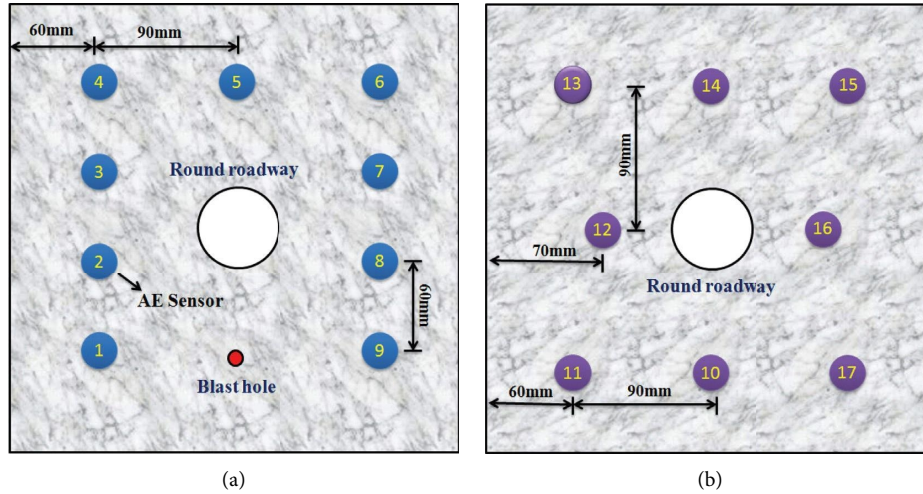
FIGURE 1: The layout of the AE sensors. (a) Sensors in the front; (b) sensors in the back.
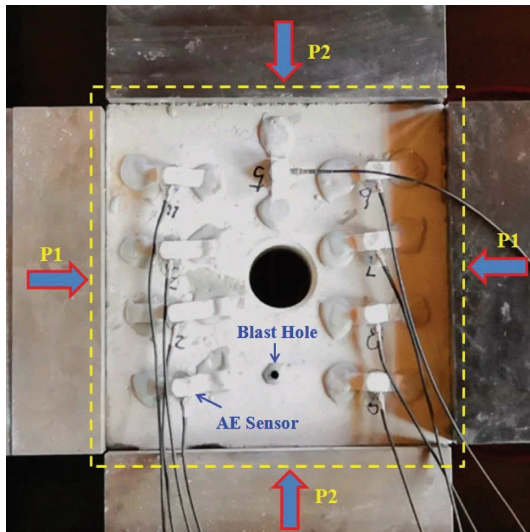

FIGURE 2: Test model and loading system.

energy levels appear in the left and right areas. After the disturbance induced by the first six blasts, many AE events aggregate on both sides of the roadway, accompanied by many events with high energy levels, while there are fewer AE events distributed in the upper and lower areas of the roadway. The distribution of AE events generated by rock mass during blasting-induced disturbance is related to the initial stress applied to the specimen. The blasting-induced disturbance intensifies microcrack initiation and accelerates the effects of the high-stress environment on crack propagation. In the later stage of stress loading, high-energy events appear in the left and right areas of the specimen, and concentrated microcracks propagate in the specimen with increasing stress, finally forming macrocracks. For the specimen with $k = 1.0$, AE events generated during the initial stress loading stage are uniformly distributed around the roadway. After the disturbance induced by the first six blasts, the distribution of AE events has no obvious directionality and is relatively uniform. At the end of the later stage of

stress loading, there are more AE events generated in the left and right areas of the roadway, which is related to the stress applied in the later stage. As for the specimens with $k = 1.2$ and 1.4, AE events generated in the test have a different distribution from those in the M1-3 specimen. The initial stress state and blasting-induced disturbance control the final failure mode and stress distribution in the rock surrounding the roadway, and the former plays a decisive role in the location and direction of the development of failure zones therein. The blasting-induced disturbance can aggravate the damage to the rock surrounding the roadway and accelerate the damage thereto.

The spatial location of AE events can represent the locus of damage to the rock and the level of aggregation of AE events directly reflects the development and severity of damage of microfractures in the rock. The distribution of levels of aggregation of AE events generated in specimens under different lateral pressure coefficients is demonstrated in Figures 5–8. For the specimen with $k = 0.8$, AE events generated in the initial stress loading process are distributed on both sides of the roadway in an elliptical shape. After the disturbance induced by the first six blasts, the level of aggregation of AE events distributed on the left and right sides of the roadway increases. After the later stage of stress loading, the range of aggregation of AE events increases. For the specimen with $k = 1.0$, AE events are uniformly distributed around the roadway throughout the test. In terms of specimens with $k = 1.2$ or 1.4, the aggregation of AE events is opposite to that at $k = 0.8$, namely that they mainly aggregate in the upper and lower areas of the roadway. The final macroscopic failures seen in the model are consistent with the level of aggregation of AE events.

5. Evolution of the Stress Field in the Rock Surrounding a Roadway

Under stress produced by an external disturbance, a rock mass is rapidly fractured or dislocates after the stress thereon reaches a certain limit, resulting in macroscopic failure of the

TABLE 1: Test schemes for blasting.

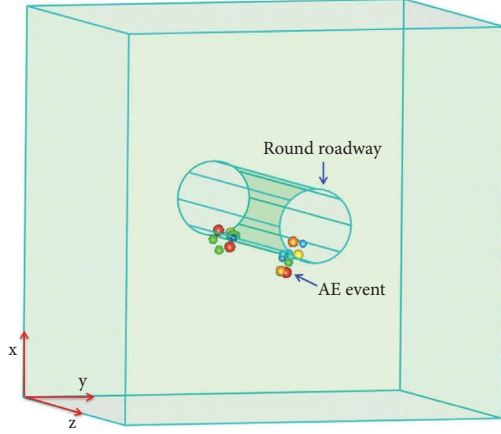| Test plan	Model	P1 (MPa)	P2 (MPa)	Blast no.	Blasting mass (g)	Lateral pressure coefficient (k)
1	M1-1, M1-2, M1-3	16	20	6	1	0.8
2	M2-1, M2-2, M2-3	16	16	6	1	1.0
3	M3-1, M3-2, M3-3	16	13.3	6	1	1.2
4	M4-1, M4-2, M4-3	16	11.4	6	1	1.4

FIGURE 3: Manual tapping test positioning result.

rock mass. Due to the anisotropy of mechanical properties and uniformity of stress applied on rock mass, it is difficult to measure the distribution and magnitude of the stresses in a rock mass directly, so it is impossible to evaluate stress states in seismic source areas with sufficient accuracy. Apparent stress, as a dynamic parameter used to describe seismic source intensity conveys abundant information about regional stress states and is thus of significance when describing the fracturing process at the seismic source. When the efficiency at the seismic source is known, the apparent stress that causes fracture or sliding of the rock mass in an area can be considered as an indirect estimate of the absolute stress in the seismic source area. Radiated microseismic energy and seismic moment are the two most important parameters required to calculate the apparent stress. The radiated microseismic energy refers to energy released in the transformation from elastic deformation to inelastic deformation of a rock mass. The seismic moment is a physical quantity used to characterize the fracture intensity of a rock mass. According to the Brune model [22], the apparent stress can be calculated as follows:

$$\sigma_{App} = \mu \frac{E_s}{M_0}, \qquad (1)$$

where μ represents the shear modulus of the rock medium in the seismic source area (generally, 3.0×10^4); E and M_0 indicate the wave energy radiated from the seismic source and seismic moment, which can be obtained through analysis and inversion of waveforms. The ratio thereof denotes the elastic wave energy radiated per unit seismic moment. The radiated microseismic energy and seismic moment can be calculated as follows:

$$E_s = 4\pi\rho\beta S_V,$$

$$M_0 = 4\sqrt{\frac{5}{2}}\pi\rho\beta^3 \Omega_0, \qquad (2)$$

where β and ρ indicate the wave velocity (km/s) and density (g/cm^3) of the rock mass, respectively. To eliminate the effects of some abnormally high values at several monitoring points on the apparent stress, logarithmic averaging proposed by Archuleta et al. [23] was utilized to calculate the mean value x of the apparent stress. The value was used to represent a single earthquake.

$$\overline{x} = \exp\left[\frac{1}{N} \sum_{i=1}^{N} \ln x_i\right],$$

$$x = \left[\frac{1}{N-1} \sum_{i=1}^{N} \left(\ln x_i - \ln\overline{x}\right)^2\right]^{1/2}, \qquad (3)$$

where N and x_i separately represent the number of sensors used in the calculation and the calculated result from the ith sensor. By calculating the apparent stress of AE events generated in each sample, the distribution of the obtained apparent stress in different stages is shown in Figure 9.

For the specimen with $k = 0.8$, after initial stress loading, stress is concentrated in the left and right areas of specimen M1-3. After the disturbance induced by the first six blasts, the apparent stress on the left and right sides of the roadway is more concentrated, and the blasting-induced disturbance intensifies crack initiation and increases the range of influence and degree of stress concentration in the high-stress area. After further stress loading, the range of influence of the high-stress area increases and is mainly distributed on the left and right-hand sides of the roadway. As for the specimen with $k = 1.0$, the apparent stress is uniformly distributed around the roadway throughout the test. For the specimens with $k = 1.2$ and 1.4, the apparent stress applied to the specimens is distributed in a contrary manner to that when $k = 0.8$, that is, the apparent stress is concentrated in the upper and lower areas of the roadway. After the blasting-induced disturbance, stress distribution patterns in the specimens are related to the initial stress applied to the specimens; because different initial stresses are applied to the specimens, the strain energy stored in different areas in the specimens is different, and more elastic strain energy is stored in the surrounding rock in a direction
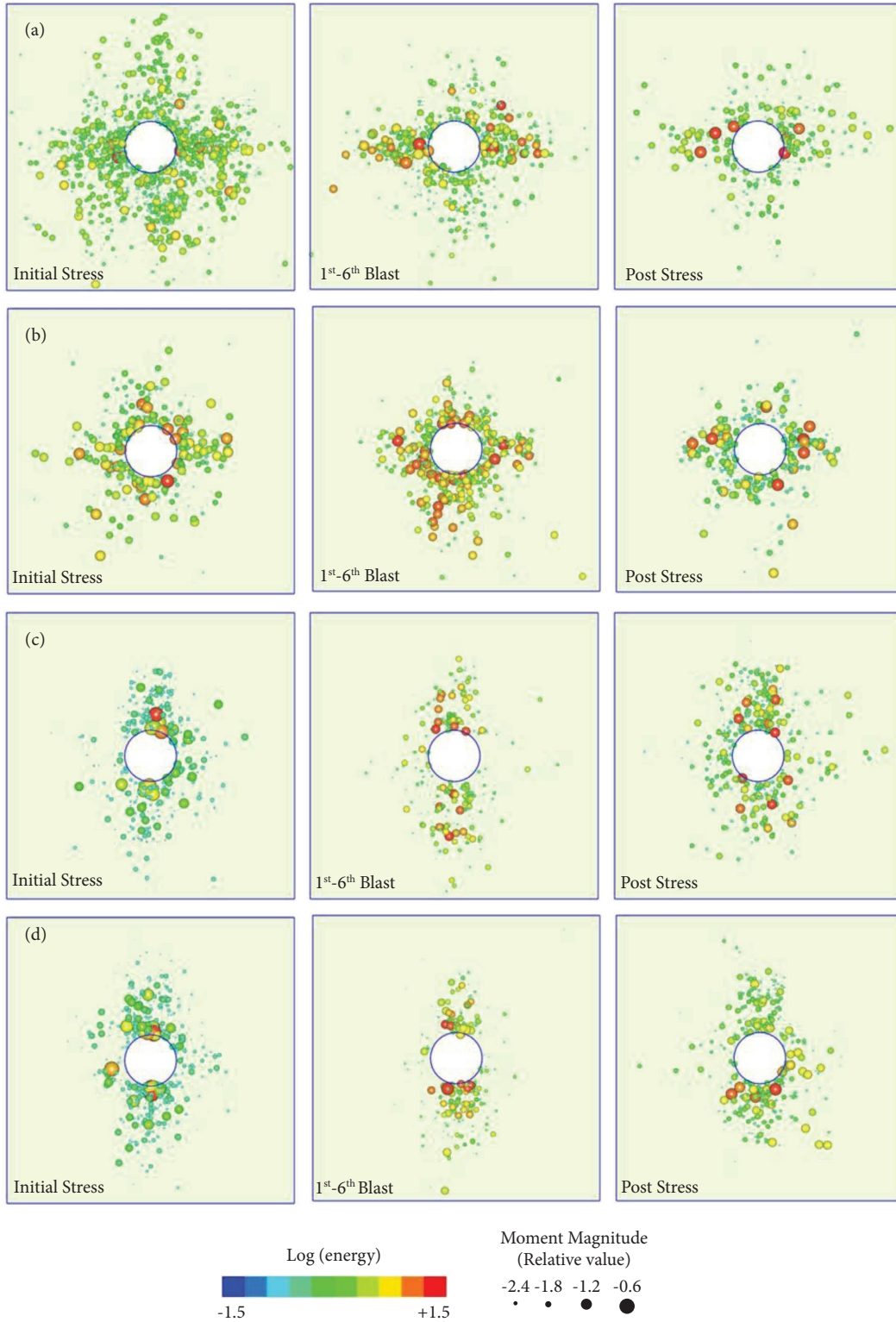
FIGURE 4: Spatial distribution of AE events. (a) M1-3; (b) M2-3; (c) M3-3; (d) M4-3.
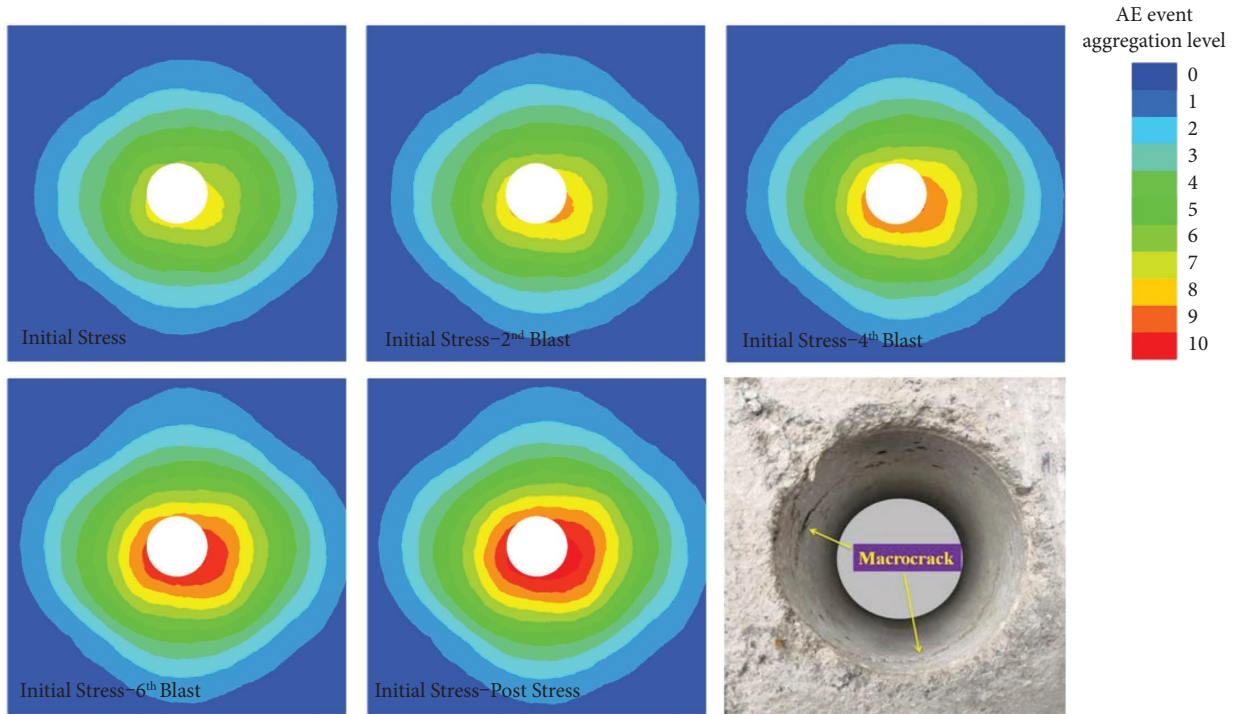
FIGURE 5: Cloud maps showing evolution of the level of aggregation of AE events in specimen M1-3 over time.
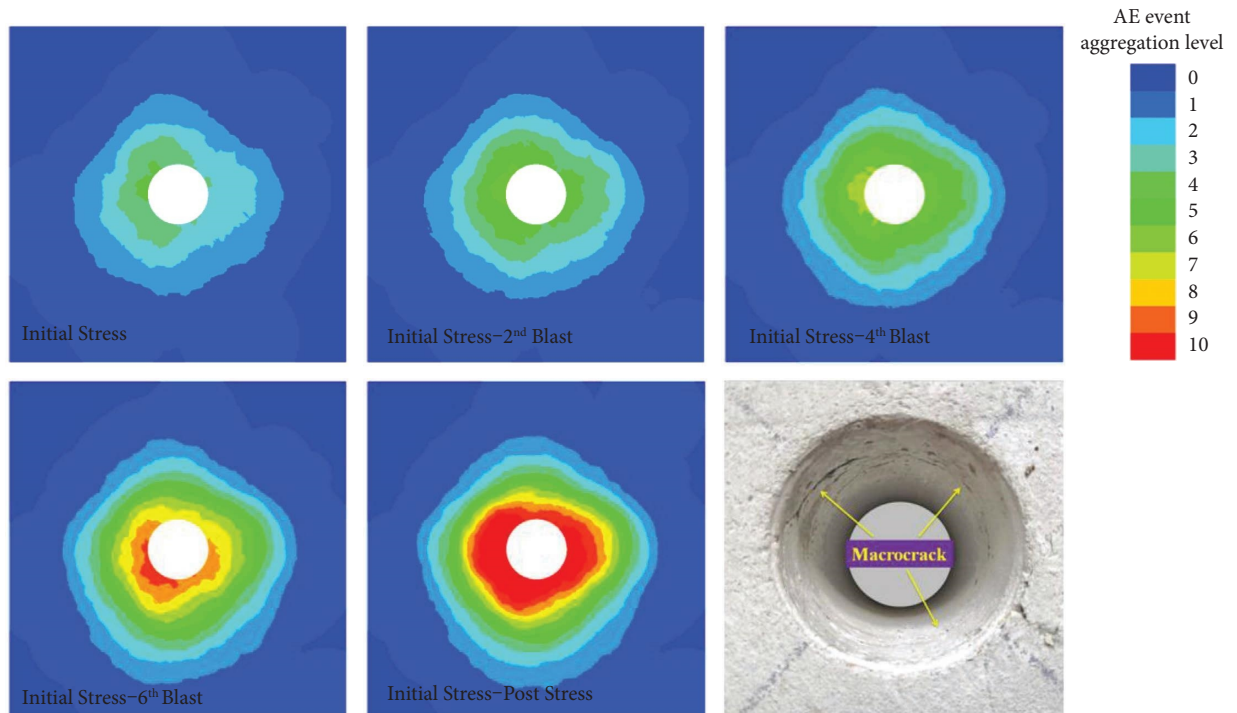

FIGURE 6: Cloud maps showing evolution of the level of aggregation of AE events in specimen M2-3 over time.

opposite to that of the applied principal stress. During blasting-induced disturbance, elastic energy stored in the specimens is gradually released, so the distribution of stress under blasting-induced disturbance is rendered directional.

6. Failure of the Rock Surrounding the Roadway

6.1. Time-Series Features of AE Events during Damage to the Rock Surrounding the Roadway. Rock damage is closely related to AE events. AE activity is a measure of the severity
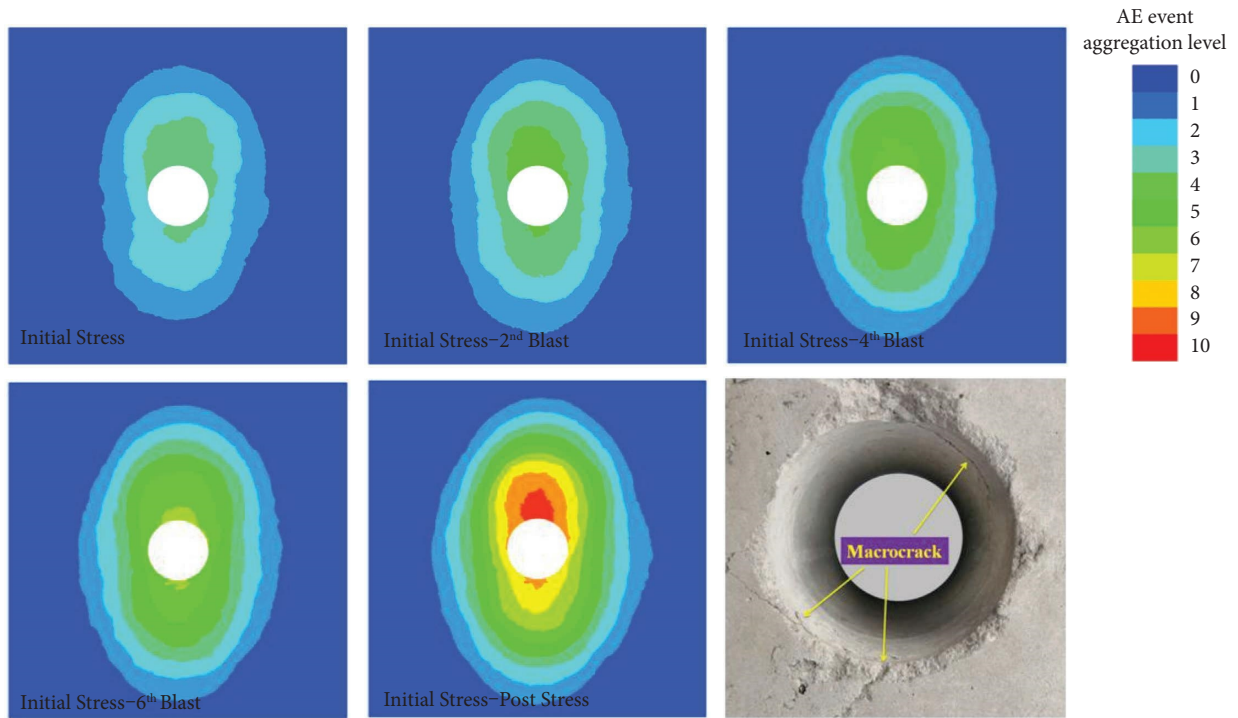
FIGURE 7: Cloud maps showing evolution of the level of aggregation of AE events in specimen M3-3 over time.
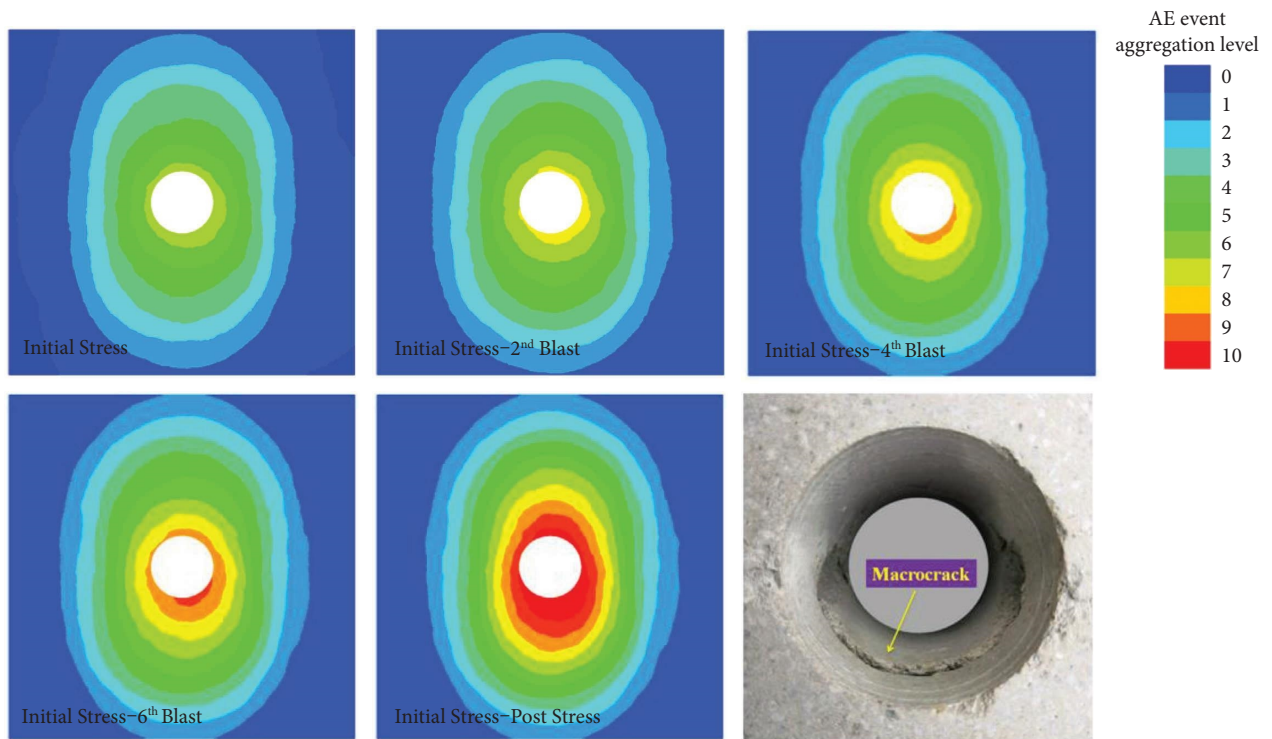

FIGURE 8: Cloud maps showing evolution of the level of aggregation of AE events in specimen M4-3 over time.

of the damage to the rock, which is the result of internal damage evolution during macrodeformation and failure. Kachanov defined the damage variable as follows:
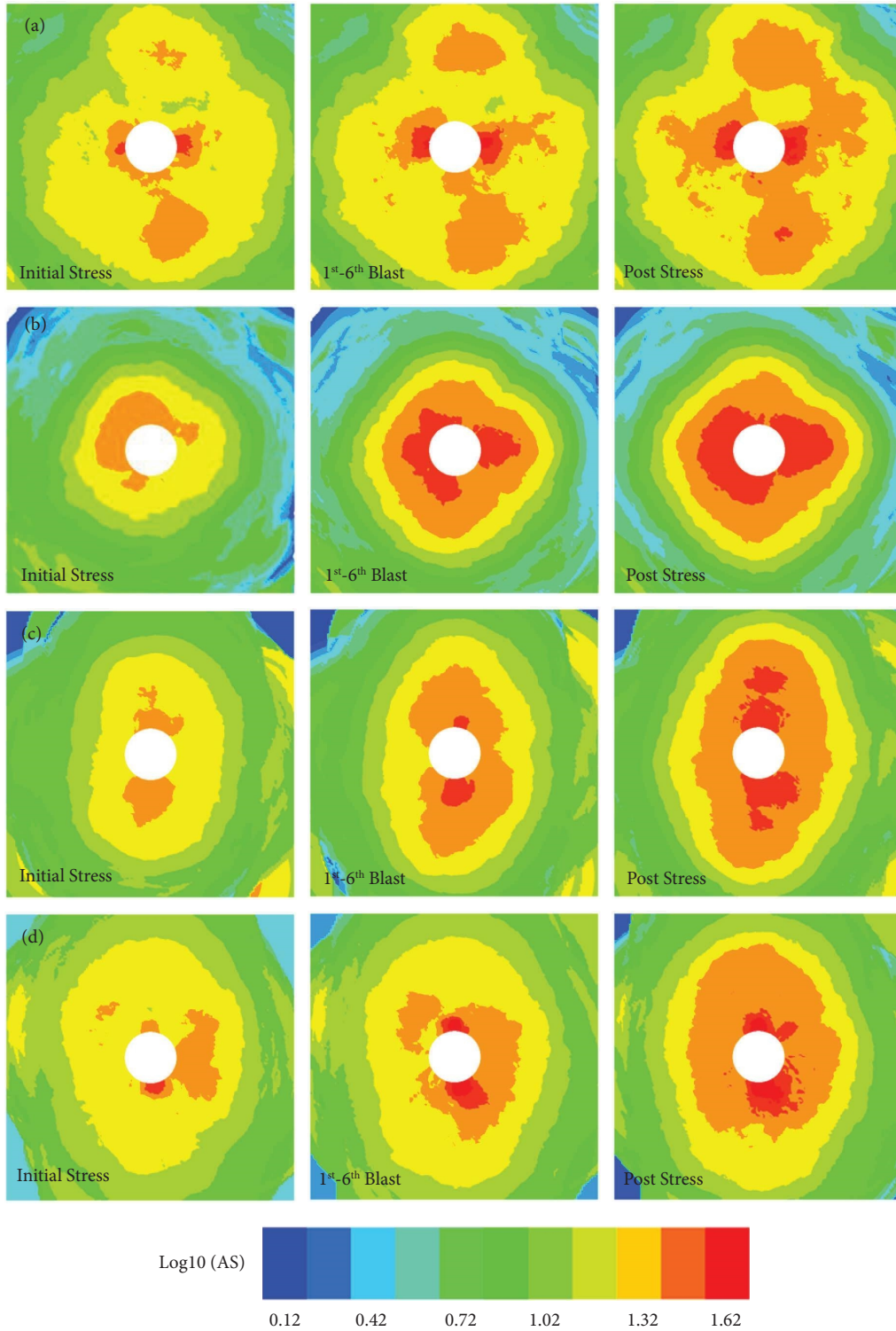
$$D = \frac{A_d}{A}, \tag{4}$$

FIGURE 9: Distribution of apparent stress with time. (a) M1-3; (b) M2-3; (c) M3-3; (d) M4-3.

where A_d and A indicate the damaged area of rock under load at macroscopic failure and area of intact rock, respectively. Assuming 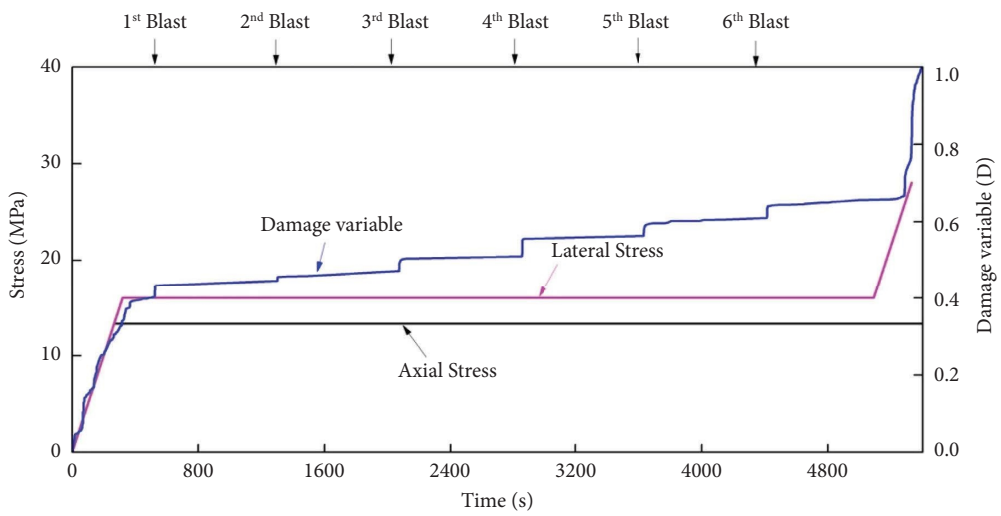the cumulative number of AE events is N_0 when the whole cross-sectional area A of the rock is completely damaged under certain conditions, the number N_W of AE events generated by microfractures per unit area is shown as follows:
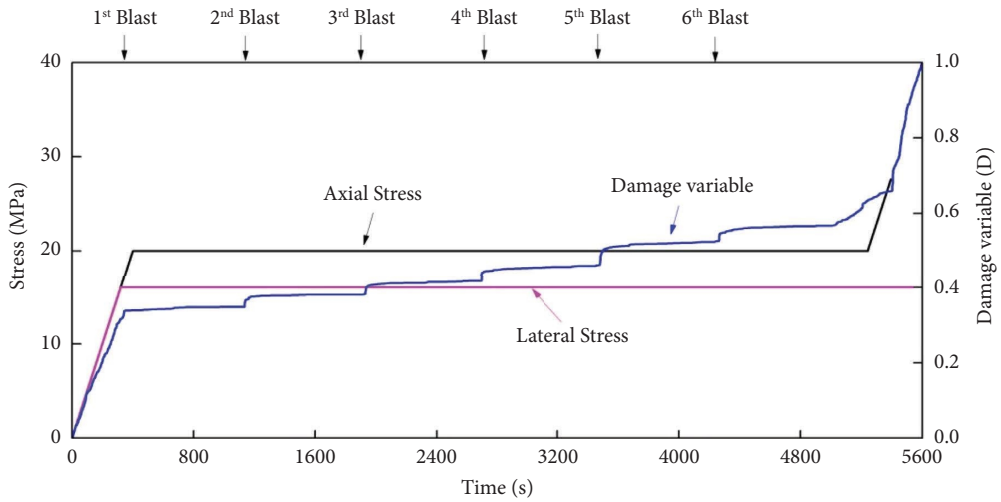
(a)
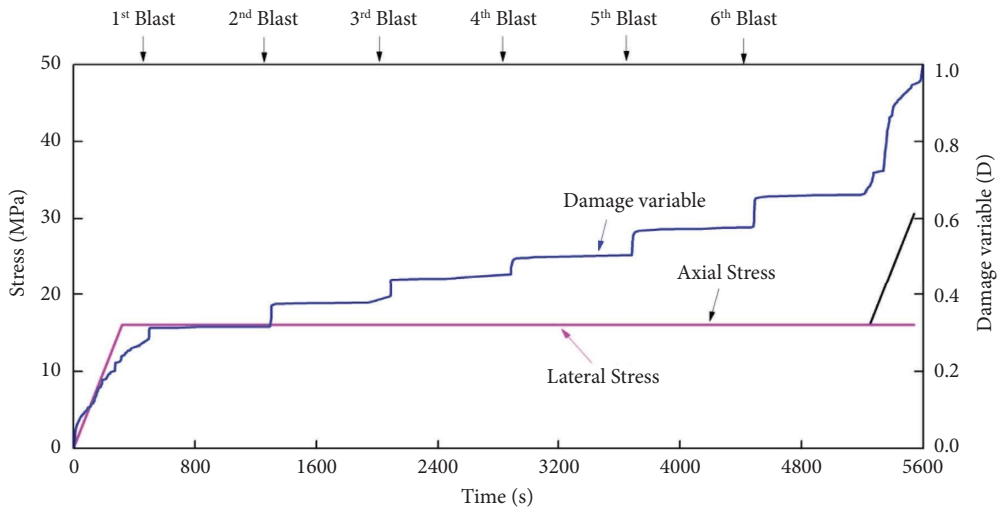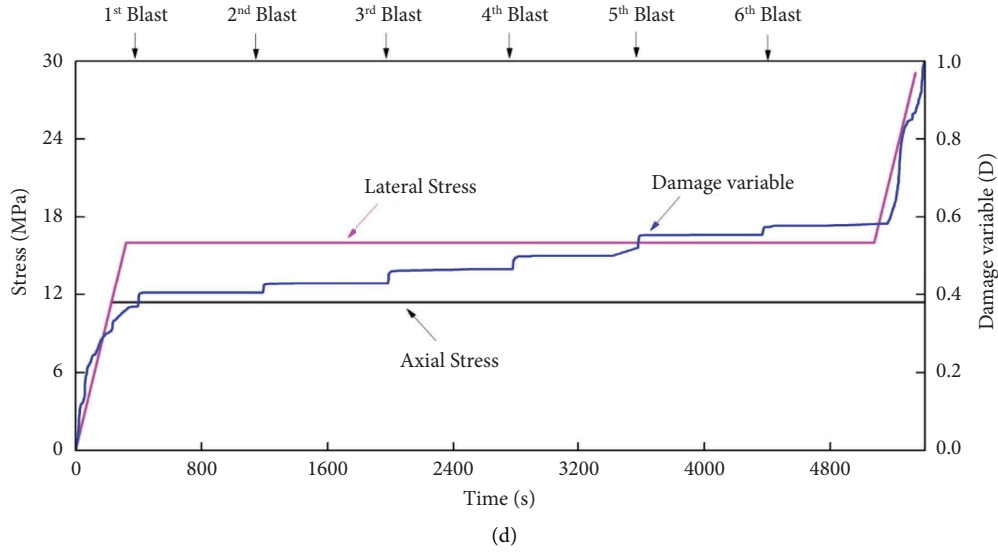

(b)

(c)

Figure 10: Continued.

FIGURE 10: Evolution of the damage variable over time. (a) M1-3; (b) M2-3; (c) M3-3; (d) M4-3.

$$N_w = \frac{N_0}{A}. \tag{5}$$

When the damaged area reaches A_d, the cumulative number of AE events is obtained as follows:

$$N_d = N_w A_d$$
$$= \frac{N_0}{A} A_d. \tag{6}$$

The damage variable of rock characterized by the ratio of the cumulative number of AE events to the total number of AE events during the whole test is expressed as follows:

$$D = \frac{N_d}{N_0}. \tag{7}$$

The ratio of the cumulative number of AE events to the total number of AE events during the whole test was taken to characterize the severity of damage to the rock in this study, thus describing damage to the specimens in the initial stress loading stage, blasting-induced disturbance stage, and later stage of stress loading. By calculating the damage variables of specimens M1-3, M2-3, M3-3, and M4-3, the evolution of the damage variables with time is demonstrated in Figure 10.

The evolution of the damage variable with time can be divided into the damage under the initial stress, blasting-induced disturbance, and stress applied in the later stage of testing. On application of the initial stress, cracks in the model constantly propagate and coalesce, and many AE events are generated. The damage variables increase reaching 0.32, 0.28, 0.40, and 0.37 for specimens M1-3 to M4-3, respectively. After entering the loading stage of blasting-induced disturbance, the high-stress environment of the specimens is conducive to microcrack initiation, propagation, and coalescence. The blasting-induced disturbance intensifies microcrack initiation and accelerates the influences of the high-stress environment on crack propagation, so that crack initiation and propagation velocities both rise after blasting. Moreover, the damage variables suddenly increase after blasting and separately reach 0.52, 0.58, 0.63, and 0.56 for specimens M1-3 to M4-3. With the increase in the number of blasts, the increase in amplitude of the damage variable rises, the mechanical properties in the model are continuously degraded, and the overall stability of the specimens decreases. Under stress loading in the later stage, microcracks in the model are constantly concentrated to form macrocracks until the model is damaged, and the damage variable associated with the AE events increases significantly. Under the joint effects of high stress in the early stage and blasting-induced disturbance, there are many microfractures formed in the model and the stability decreases. Furthermore, damage to the test block is imminent, such that even a small change in the stress thereon may lead to the failure of the whole model.

7. Conclusions

(1) The initial stress state and blasting-induced disturbance control the final failure mode and stress distribution in the rock surrounding the roadway, and the former plays a decisive role in the location and direction of the development of failure zones therein. The high-stress areas provide a favorable environment for crack initiation and accelerate damage accumulation and macrofracture formation in the rock mass. The blasting-induced disturbance can increase the severity of damage to the rock surrounding the roadway and accelerate its failure.

(2) When different stresses are applied to the specimens, the strain energy stored in different areas of the specimens is different, and more elastic strain energy is stored in the rock surrounding the roadway in the direction opposite to that of the applied principal stress. Under blasting-induced disturbance, the

elastic energy stored in the specimens is released, and the distribution of apparent stress is rendered directional.

(3) As the number of blasting events increases, the damage variable and level of aggregation of AE events suddenly increase. Under frequent blasting-induced disturbances, the mechanical properties of the specimens degrade and the overall stability of the rock decreases. The trends in damage variable and level of aggregation of AE events can reflect the process whereby microcracks in the rock mass propagate and coalesce, leading to macroscopic failure.

Data Availability

The data that support the findings of this study are available from the corresponding author upon reasonable request.

Conflicts of Interest

The authors declare that there are no conflicts of interest.

Acknowledgments

References

[1] J. Martino and N. Chandler, "Excavation-induced damage studies at the underground research laboratory," *International Journal of Rock Mechanics and Mining Sciences*, vol. 41, no. 8, pp. 1413–1426, 2004.

[2] J. Yang, Q. Jiang, Q. Zhang, and J. Zhao, "Dynamic stress adjustment and rock damage during blasting excavation in a deep-buried circular tunnel," *Tunnelling and Underground Space Technology*, vol. 71, pp. 591–604, 2018.

[3] J. Yang, W. Lu, M. Chen, P. Yan, and C. Zhou, "Microseism induced by transient release of in situ stress during deep rock mass excavation by blasting," *Rock Mechanics and Rock Engineering*, vol. 46, no. 4, pp. 859–875, 2013.

[4] X.-T. Feng, Y. Yu, G.-L. Feng, Y. X. Xiao, B. Chen, and Q. Jiang, "Fractal behaviour of the microseismic energy associated with immediate rockbursts in deep, hard rock tunnels," *Tunnelling and Underground Space Technology*, vol. 51, pp. 98–107, 2016.

[5] L. Yuan-hui, L. Gang, X. Shi-da, and W. Da-wei, "The spatial-temporal evolution law of microseismic activities in the failure process of deep rock masses," *Journal of Applied Geophysics*, vol. 154, pp. 1–10, 2018.

[6] X. Zheng, *Research on Blasting Vibration Effect of Underground Mining in Daye Iron Mine*, China University of Geosciences, Wuhan, China, 2010.

[7] X. Beijing, D. Ai, and Y. Yang, "Crack detection and evolution law for rock mass under SHPB impact tests," *Shock and Vibration*, vol. 2019, no. 2, Article ID 3956749, 12 pages, 2019.

[8] D. Ai, Y. Zhao, Q. Wang, and C. Li, "Experimental and numerical investigation of crack propagation and dynamic properties of rock in SHPB indirect tension test," *International Journal of Impact Engineering*, vol. 126, no. 4, pp. 135–146, 2019.

[9] R. Chen, W. Yao, F. Lu, and K. Xia, "Evaluation of the stress equilibrium condition in axially constrained triaxial SHPB tests," *Experimental Mechanics*, vol. 58, no. 3, pp. 527–531, 2018.

[10] J. Li, L. Rong, H. Li, and S. N. Hong, "An SHPB test study on stress wave energy attenuation in jointed rock masses," *Rock Mechanics and Rock Engineering*, vol. 52, no. 2, pp. 403–420, 2019.

[11] R. Christensen, S. Swanson, and W. Brown, "Split-Hopkinson-bar tests on rock under confining pressure," *Experimental Mechanics*, vol. 12, no. 11, pp. 508–513, 1972.

[12] Z.-L. Zhou, Y. Zhao, Y.-H. Jiang, Y. Zou, X. Cai, and D. Y. Li, "Dynamic behavior of rock during its post failure stage in SHPB tests," *Transactions of Nonferrous Metals Society of China*, vol. 27, no. 1, pp. 184–196, 2017.

[13] H.-B. Du, F. Dai, Y. Xu, Y. Liu, and H. Xu, "Numerical investigation on the dynamic strength and failure behavior of rocks under hydrostatic confinement in SHPB testing," *International Journal of Rock Mechanics and Mining Sciences*, vol. 108, no. 8, pp. 43–57, 2018.

[14] B. Duan, H. Xia, and X. Yang, "Impacts of bench blasting vibration on the stability of the surrounding rock masses of roadways," *Tunnelling and Underground Space Technology*, vol. 71, pp. 605–622, 2018.

[15] N. Jiang and C. Zhou, "Blasting vibration safety criterion for a tunnel liner structure," *Tunnelling and Underground Space Technology*, vol. 32, pp. 52–57, 2012.

[16] X. Li, C. Li, W. Cao, and M. Tao, "Dynamic stress concentration and energy evolution of deep-buried tunnels under blasting loads," *International Journal of Rock Mechanics and Mining Sciences*, vol. 104, no. 4, pp. 131–146, 2018.

[17] L. Dexing, W. Enyuan, K. Xiangguo, J. Haishan, W. Dongming, and A. Muhammad, "Damage precursor of construction rocks under uniaxial cyclic loading tests analyzed by acoustic emission," *Construction and Building Materials*, vol. 206, no. 5, pp. 169–178, 2019.

[18] S. Liu, X. Li, Z. Li, P. Chen, X. Yang, and Y. Liu, "Energy distribution and fractal characterization of acoustic emission (AE) during coal deformation and fracturing," *Measurement*, vol. 136, pp. 122–131, 2019.

[19] H. Song, Y. Zhao, Y. Jiang, and J. Wang, "Scale effect on the anisotropy of acoustic emission in coal," *Shock and Vibration*, vol. 2018, Article ID 8386428, 11 pages, 2018.

[20] G. Su, Y. Shi, X. Feng, J. Jiang, J. Zhang, and Q. Jiang, "True-triaxial experimental study of the evolutionary features of the acoustic emissions and sounds of rockburst processes," *Rock Mechanics and Rock Engineering*, vol. 51, no. 2, pp. 375–389, 2018.

[21] L. Weng, X. Li, A. Taheri, Q. Wu, and X. Xie, "Fracture evolution around a cavity in brittle rock under uniaxial compression and coupled static–dynamic loads," *Rock Mechanics and Rock Engineering*, vol. 51, no. 2, pp. 531–545, 2018.

[22] J. N. Brune, "Tectonic stress and the spectra of seismic shear waves from earthquakes," *Journal of Geophysical Research*, vol. 75, no. 26, pp. 4997–5009, 1970.

[23] R. J. Archuleta, E. Cranswick, C. Mueller, and P. Spudich, "Source parameters of the 1980 Mammoth Lakes, California, earthquake sequence," *Journal of Geophysical Research: Solid Earth*, vol. 87, no. 6, pp. 4595–4607, 1982.